

Article

Piranha Solution-Assisted Surface Engineering Enables Silicon Nanocrystals with Superior Wettability and Lithium Storage

Tingting Li¹, Yangfan Li¹, Fan Zhang¹, Naiwen Liang¹, Jiang Yin¹, Haihong Zhao^{1,*}, Yahui Yang¹, Bo Chen^{2,*} and Lishan Yang^{1,*}

¹ National and Local Joint Engineering Laboratory for New Petrochemical Materials and Fine Utilization of Resources, Key Laboratory of the Assembly and Application of Organic Functional Molecules of Hunan Province, Hunan Normal University, Changsha 410081, China

² State Key Laboratory of Organic Electronics and Information Displays & Jiangsu Key Laboratory for Biosensors, Institute of Advanced Materials (IAM), School of Chemistry and Life Sciences, Nanjing University of Posts and Telecommunications, Nanjing 210023, China

* Correspondence: zhh_1998@163.com (H.Z.); iambchen@njupt.edu.cn (B.C.); lsyang@hunnu.edu.cn (L.Y.); Tel.: +86-731-88872531 (L.Y.)

Abstract: Silicon anodes with a high theoretical capacity possess great potential applications in power batteries for electric vehicles, while their volume expansion always leads to crystal pulverization and electrode polarization. An ideal solution to alleviate such pulverization and polarization of silicon crystals is to simultaneously use nano-sized silicon crystals and introduce high viscosity and elasticity polymer binders. This work has achieved the adjustable introduction of hydroxyl groups to silicon nanocrystals under the optimal reaction temperature (e.g., 80 °C) and appropriate piranha solution composition (e.g., H₂SO₄/H₂O₂ = 3:1 v/v), ultimately forming an amorphous coating layer of ~1.3 nm on the silicon surface. The optimized silicon anode exhibits superior electrochemical performance (with an initial Coulombic efficiency of 85.5%; 1121.4 mA h g⁻¹ at 1 A g⁻¹ after 200 cycles) and improved hydrophilicity. The introduced hydroxyl groups significantly enhance the hydrophilicity of silicon in the electrolyte and the electrochemical activity of the silicon anodes. The hydroxyl groups achieve stronger bonding between silicon and polymer binders, ultimately improving the mechanical strength and stability of the electrode. The introduction of hydrophilic functional groups on the surface of silicon crystals can be explored as an active strategy to solve the above issues. This surface engineering method could be extended to more fields of infiltrating silicon-based functional materials.

Keywords: lithium-ion batteries; silicon anode; nanocrystals; surface engineering; piranha solution



Citation: Li, T.; Li, Y.; Zhang, F.; Liang, N.; Yin, J.; Zhao, H.; Yang, Y.; Chen, B.; Yang, L. Piranha Solution-Assisted Surface Engineering Enables Silicon Nanocrystals with Superior Wettability and Lithium Storage. *Crystals* **2023**, *13*, 1127. <https://doi.org/10.3390/cryst13071127>

Academic Editor: Xiaofei Yang

Received: 26 June 2023

Revised: 16 July 2023

Accepted: 17 July 2023

Published: 19 July 2023



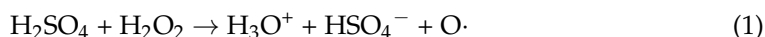
Copyright: © 2023 by the authors. Licensee MDPI, Basel, Switzerland. This article is an open access article distributed under the terms and conditions of the Creative Commons Attribution (CC BY) license (<https://creativecommons.org/licenses/by/4.0/>).

1. Introduction

Over the past few years, lithium-ion batteries (LIBs) have become one choice for portable electronic devices due to their extreme long cycling life, flexibility, and lightweight design [1–4]. Silicon (Si), as one of the most abundant elements in the earth, is considered as a candidate anode material for the next generation of high energy density LIBs due to its high theoretical specific capacity (4200 mA h g⁻¹) (Li₂₂Si₅), suitable working potential (0.2 V vs. Li/Li⁺), and high energy density [5–11]. In addition, Si is less likely to cause surface lithium precipitation during the lithiation/delithiation process, which could suppress the occurrence of lithium dendrites to some extent, resulting in better safety performance than graphite [12–14]. However, the inevitable huge volume expansion (up to 300%) during the Li⁺ insertion/deinsertion process, resulting in severe cracking of active materials and electrical contact losses, accompanied rapid electrode disassembly and capacity degradation. In addition, the consequently formed unstable solid electrolyte interphase (SEI) film is accompanied by subsequent continuous consumption of electrolytes and makes the long-term cycling of Si anodes more difficult [15–18].

To solve the issues mentioned above, Si-based materials with nanosized structures are commonly used. Nanocrystals-Si can shorten the transport path of Li^+ , reducing potential polarization and providing sufficient adjustment surfaces to effectively release the stress caused by drastic changes in lattice volume, preventing the degradation of electrode structure [19–23]. Commercial silicon is mainly obtained by using the external energy of silane to decompose into silicon and hydrogen in a hydrogen atmosphere, which is quickly condensed. Due to its easy operation and low cost, its mass production and commercialization can easily be achieved. However, the problems of aggregation and hydrophobicity of commercial silicon make further modification of commercial silicon powder difficult [24,25]. Surface treatment of commercial nano Si powders is performed to improve the interface and facilitate in situ coating modification on its surface to further enhance the performance of Si-based materials. Therefore, surface engineering treatment of Si materials is particularly important.

Piranha solution is a strong oxidant typically composed of concentrated sulfuric acid (H_2SO_4) and hydrogen peroxide (H_2O_2), known for altering the surface properties of polymers. This is due to the chemical reaction between H_2SO_4 and H_2O_2 in the piranha solution, which produces hydrated hydrogen ions (H_3O^+), hydrogen sulfate ions (HSO_4^-), and active atomic oxygen ($\text{O}\cdot$), as shown in Formula (1) [26]. The formation of active atomic oxygen is the key to the formation of silanol groups on the surface of Si particles treated with piranha solution. In this regard, Koh and co-workers used different acids and H_2O_2 at a weight ratio of 3:1 to attack Si-CH₃ on the surface of polydimethylsiloxane to generate silanol groups to improve its hydrophilicity [26]. In addition, a large number of studies have found that the functional groups on the surface of Si are particularly important for subsequent coating, as well as for the modification of binders and electrolytes. Guo and co-workers synthesized nano-Si with an amorphous protective layer and rich hydroxyl groups by piranha solution ($\text{H}_2\text{SO}_4/\text{H}_2\text{O}_2 = 7:3$ v/v for 2 h at 80 °C), thus obtaining robust Si-based anode, which is attributed to the excellent combination by esterification reaction between the designed novel binders and hydroxyl groups. [27]. Jung and co-workers used piranha solution ($\text{H}_2\text{SO}_4/\text{H}_2\text{O}_2 = 3:1$ v/v for 1–2 h at 85 °C) to introduce hydrophilic SiO_x into the surface of Si, which could better composite with the designed graphene oxide polyacrylic acid [28]. Zhu and co-workers used piranha solution ($\text{H}_2\text{SO}_4/\text{H}_2\text{O}_2 = 3:1$ v/v for 1 h in boiling) to introduce hydroxyl groups into Si nanowires, and then coated them with graphene [29]. It can be observed that these studies used different surface treatment conditions, while there is no work exploring the effect of acid treatment temperature on piranha currently.



In this work, we achieved the adjustable introduction of hydroxyl groups to Si nanocrystals under the optimal reaction temperature (e.g., 80 °C) and appropriate piranha solution composition (e.g., $\text{H}_2\text{SO}_4/\text{H}_2\text{O}_2 = 3:1$ v/v), ultimately forming an amorphous coating layer of ~1.3 nm on the Si surface, which is shown in Figure 1. The optimized Si anode exhibited superior electrochemical performance (with an initial Coulombic efficiency of 85.5%; a reversible specific capacity of 1121.4 mA h g⁻¹ at 1 A g⁻¹ after 200 cycles) and improved hydrophilicity. The introduced hydroxyl groups significantly enhanced the hydrophilicity of Si in the electrolytes and binders, thus increasing the electrochemical activity of the Si anodes. In addition, hydrogen bonds formed between hydroxyl groups and binders ultimately enhanced the mechanical strength and stability of the electrode. This work summarized the optimal treatment temperature for Si materials with piranha solution, which can be widely used in the pretreatment of hydrophobic materials.

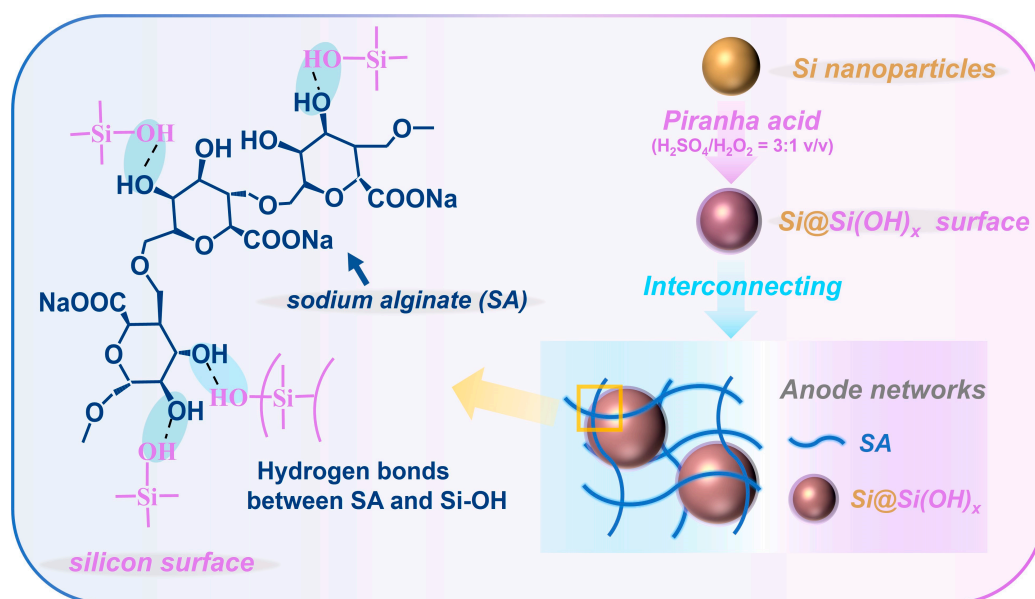


Figure 1. The preparation steps and the inter-structures of the Si@Si(OH)_x anode.

2. Materials and Methods

2.1. Preparation of Si@(OH)_x

Commercial nanosized-Si powders were purchased from Xiang Tian Nano (Shanghai, China). Typically, 2 g nanosized-Si powders were magnetically stirred in the 80 mL piranha solution (H₂SO₄/H₂O₂ = 3:1 v/v) at different temperatures (e.g., 65 °C, 80 °C, and 95 °C) for 2 h. After that, the modified products were diluted with deionized water, then centrifugally washed with deionized water three times. Then, after washing with ethanol solution, the obtained products dried in an oven at 80 °C for 12 h. The Si crystals treated at different temperatures were named as Si@Si(OH)_x-1 (65 °C), Si@Si(OH)_x-2 (80 °C), and Si@Si(OH)_x-3 (95 °C), respectively.

2.2. Materials Characterization

The morphologies and elemental composition of materials were characterized by transmission electron microscope (TEM, FEI Talos F200x G2, Thermo Fisher Scientific, Hillsboro, OR, USA) and scanning electron microscope (SEM, ZEISS Sigma 300, Carl Zeiss AG, Oberkochen, Germany). X-ray photoelectron spectroscopy (XPS, Thermo Scientific K-Alpha, Thermo Fisher Scientific, Waltham, MA, USA) was utilized to measure the elements and components on the surface of materials. The phase and crystallinity of materials were measured by powder X-ray Diffraction (XRD Bruker D8 X-ray diffractometer, Bruker Corporation, Billerica, MA, USA, Cu K α radiation, $\lambda = 1.5406 \text{ \AA}$, operated from 5° to 90° (2 θ)) and Raman spectroscopy (HORIBA Scientific LabRAM, HORIBA, Kyoto, Japan) with a 532 nm excitation laser. The functional groups of materials were characterized by Fourier transform infrared spectroscopy (FTIR, Thermo Scientific Nicolet iS20, Thermo Fisher Scientific, Waltham, MA, USA) from 400 to 4000 cm⁻¹ (KBr tablet). The hydrophilicity and contact angle of samples were analyzed by spinning drop interface tensiometer (TX500 TM, KINO, Boston, MA, USA).

2.3. Electrochemical Measurements

The electrochemical performances of materials were measured by assembling 2032 coin-type half cells. The active materials, super-P and sodium alginate (SA) with a weight ratio of 70:15:15 were mixed in deionized (DI) water to form a homogenous slurry. The obtained slurry was then painted onto copper foils with a blade, then dried at 100 °C for 12 h. For each electrode, the mass loading of active materials was controlled at around 1 mg cm⁻². In the half cells, metal lithium foils were used as the counter electrode in an Ar-filled glove

box (O_2 and H_2O less than 0.1 ppm). The electrolyte consists of 1 M $LiPF_6$ dissolved in EC:DEC = 1:1 (volume ratio) with 5% FEC. The electrochemical impedance spectroscopy (EIS) and cyclic voltammetry (CV) were performed on an electrochemical workstation (CHI 760E, Shanghai, China). EIS was tested under a frequency range of 100k–0.01 Hz. CV characterizations were measured with a potential range of 0.01–2.0 V (scan rate: 0.1 mV s^{-1}). The galvanostatic discharge-charge tests were performed on a Neware CT-4008 battery system (Bellevue, WA, USA) at 28°C (voltage range: 0.01–2 V).

3. Results

The XRD patterns are shown in Figure 2a. The commercial Si powders possess obvious Si characteristic peaks, and their diffraction peaks coincide with the peak positions of the standard card of Si (PDF#27-1402), where the peak positions of 28.4° , 47.3° , 56.1° , 69.1° , and 76.4° correspond to crystalline Si (111), (220), (311), (400), and (331) crystal planes [27,30]. The treated Si ($Si@Si(OH)_x$) powders possess peaks at the same positions with Si, while the peaks intensity was slightly smaller than the commercial Si powders, which may be due to the influence of the amorphous $Si(OH)_x$ surface introduced by piranha solution on the surface of Si. Additionally, Figure 2a demonstrates that the peak intensity gradually decreases as the treatment temperature of the piranha solution increases, which could be apparently observed in Figure S1. The particle sizes of different samples calculated based on the Scherrer formula are shown in Table S1. As the processing temperature increases, the corresponding particle sizes calculated by the formula gradually decrease, indicating the improvements in the dispersion of Si. Meanwhile, the Raman spectra of the samples are shown in Figure S2. The Si and $Si@Si(OH)_x-2$ powders have characteristic peaks of Si at 496 cm^{-1} and 925 cm^{-1} , while the peak intensity of the treated sample was slightly smaller than raw materials, which is consistent with the XRD results.

To investigate the surface functionalization effect of Si treated by piranha solution, FTIR spectra of the samples are displayed in Figure 2b. Both Si and serials of $Si@Si(OH)_x$ powders possess the characteristic peaks of hydroxyl ($-OH$) and Si-O bond at 3435 cm^{-1} and 1211 cm^{-1} [31–35], which may be caused by the exposure of Si materials to air. However, the treated Si materials at different temperatures show a weak characteristic peak of Si-OH at 965 cm^{-1} [32], which proved that the treatment of piranha solution successfully realized the introduction of $Si(OH)_x$ surface in Si. To further clarify the details of the surface of Si treated with different temperature piranha solutions, we performed XPS characterizations of the Si and treated samples. As shown in Figure 2c, the Si 2p spectra show that both the Si and treated Si possess the two peaks at 99.06 and 99.68 eV, corresponding to Si and Si-Si bonds. The intensities of these two peaks corresponding to pure Si in Si without introducing $Si(OH)_x$ surface are significantly higher than that of treated Si. Moreover, with the increase in treatment temperature, their intensities correspondingly decrease. The peaks at 100.38, 102.39, and 103.19 eV correspond to Si-O bond, Si-OH bond, and SiO_2 are observed in Si, indicating that the surface of Si has a natural silicon-oxygen layer [27]. It could be seen that with the increase in treatment temperature, the Si-OH bond intensity significantly increases, indicating that the controllable preparation of $Si(OH)_x$ surface could be achieved by adjusting the temperature. The introduction of $Si(OH)_x$ surface could form hydrogen bonds with SA to effectively strengthen the bond between Si and binders, thereby increasing the stability of the electrode. In C 1s, the samples possess two characteristic peaks at 284.8 and 286.5 eV, corresponding to C-C and C-O-C bonds. It is noticed that compared with commercial Si, the treated Si powders with piranha solution appeared O=C=O characteristic bond at 288.8 eV, which is consistent with the results in O 1s. The $Si@Si(OH)_x$ powders exhibit an obvious peak at 535.5 eV, corresponding to C=O bond, which is absent in Si. We speculate that this may be through the treatment of Si powders, they absorb carbon dioxide in exposed air. Excluding the aforementioned C=O bond, the samples all have three peaks at 531.6, 532.2, and 533 eV, corresponding to C-O, Si-O, and SiO_2 bond. Compared with Si, the intensities of SiO_2 are smaller, which corresponds to results in Si 2p.

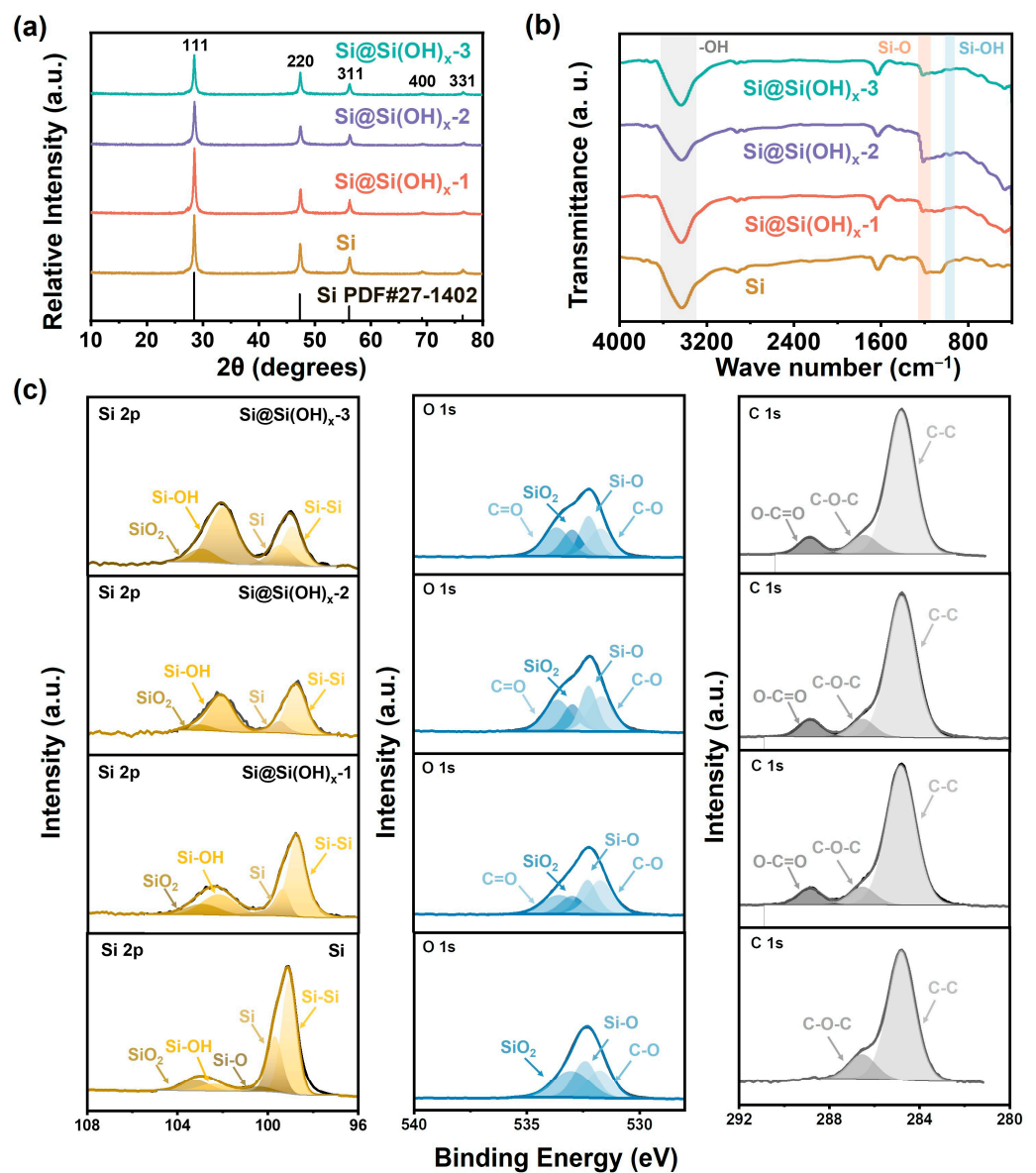


Figure 2. (a) XRD patterns, (b) FTIR spectra, and (c) XPS spectra of Si, Si@Si(OH)_{x-1}, Si@Si(OH)_{x-2}, and Si@Si(OH)_{x-3} nanoparticles.

The SEM images of samples are displayed in Figure 3. After piranha solution treatment, the agglomeration phenomena of particles in all three treated-samples, especially Si@Si(OH)_{x-2} and Si@Si(OH)_{x-3} nanoparticles, were alleviated. This is because the hydroxyl functions introduced through the treatment of piranha solution improve their hydrophilicity, making the Si more easily dispersed in solutions and reducing agglomeration. In order to further verify whether the hydrophilicity of Si powders treated with piranha solution is improved, we performed contact angle tests between the Si and the Si@Si(OH)_x electrode, which is shown in Figure S3. Compared with the contact angle (23.78°) of Si electrode, Si@Si(OH)_{x-1} (19.15°), Si@Si(OH)_{x-2} (16.34°), and Si@Si(OH)_{x-3} (18.92°) electrodes are much smaller than the contact angle of the raw materials, indicating that the hydrophilicity of Si powders treated with piranha solution is significantly enhanced.

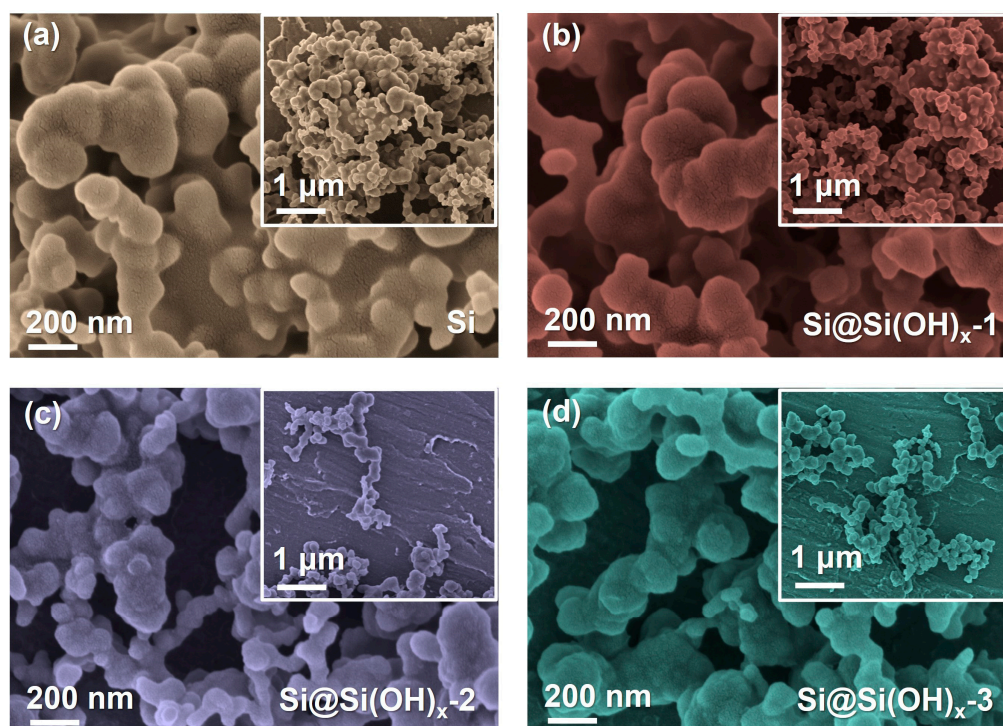


Figure 3. SEM images of (a) the pristine Si particles, (b) the modified Si@Si(OH)_{x-1} nanoparticles, (c) the modified Si@Si(OH)_{x-2} nanoparticles, and (d) the modified Si@Si(OH)_{x-3} nanoparticles by piranha solution.

In order to further observe the morphologies, we characterized the Si and Si@Si(OH)_{x-2} by TEM, which are shown in Figure 4. The spherical structures could be observed in both Si powders and Si@Si(OH)_{x-2} powders. The Si powders without surface treatment of piranha solution have serious accumulation, and the particle sizes of Si@Si(OH)_{x-2} are slightly smaller. Distinct lattice fringes can be observed for all materials in high resolution transmission electron microscopy (HRTEM), and the measured 0.31 nm lattice spacing corresponds to the (111) crystal plane of Si, confirming the existence of Si phase. From the selected area electron diffraction (SAED) patterns of Si and Si@Si(OH)_{x-2} , it shows that the Si powders used are polycrystalline materials, and both materials have obvious diffraction rings at the crystal faces of (111), (220), and (311), which indicates that the surface engineering treatment of the piranha solution does not change the crystal structures of Si. In addition, as shown in Figure 4(b₂), the amorphous layer range on the surface of the modified Si@Si(OH)_{x-2} powders increases, and the thickness increases from ~0.87 nm of Si powders to ~1.3 nm, further indicating that piranha solution successfully introduced a new amorphous layer to the Si surface. It is clear from the energy dispersive spectrometer (EDS) element mappings of Si@Si(OH)_{x-2} powders (Figure 4c) that the O element is evenly allocated in the external layer of the Si nanoparticles, which is consistent with the XPS results.

The electrochemical performances of Si and serials of Si@Si(OH)_x samples were tested in half cells, which are shown in Figure 5. Figure 5a shows the cycling performances of Si, Si@Si(OH)_{x-1} , Si@Si(OH)_{x-2} , and Si@Si(OH)_{x-3} anodes at a current density of 1.0 A g^{-1} . Compared with the raw Si, the anode materials treated with piranha solution exhibit excellent cycling performance after 200 cycles. The discharge capacity of the first cycle of the Si@Si(OH)_{x-2} anode is $3394.7 \text{ mA h g}^{-1}$, and the discharge capacity of the 200th cycle is $1121.4 \text{ mA h g}^{-1}$, which are higher than Si@Si(OH)_{x-1} anode ($3095.5 \text{ mA h g}^{-1}$ in the first cycle and $924.3 \text{ mA h g}^{-1}$ after 200th cycles) and Si@Si(OH)_{x-3} anode ($2935.0 \text{ mA h g}^{-1}$ in the first cycle and $992.3 \text{ mA h g}^{-1}$ after 200th cycles). Figure S4 compares the constant current charge–discharge curves of various anodes in the first cycle and the 100th cycle. The initial Coulomb efficiencies of Si, Si@Si(OH)_{x-1} , Si@Si(OH)_{x-2} , and Si@Si(OH)_{x-3} anodes were 81.4%, 84.9%, 85.5% and 80.5%, respectively, and Si@Si(OH)_{x-2} anode possesses

the highest initial Coulomb efficiency. In addition, compared with Si, Si@Si(OH)_{x-1} and Si@Si(OH)_{x-3} anodes, the Si@Si(OH)_{x-2} anode exhibits the highest discharge platform and the lowest charging platform, meaning excellent electrochemical performances, which is consistent with the results of Figure 4a. The rate performances of the serials samples are measured by ramping the current from 0.2 to 5 A g⁻¹, which are shown in Figure 5b. The rate performance of Si@Si(OH)_{x-2} anode is much better than that of Si, Si@Si(OH)_{x-1}, and Si@Si(OH)_{x-3}, with a high reversible specific capacity of 1127.6 mA h g⁻¹ even at a high rate of 5 A g⁻¹.

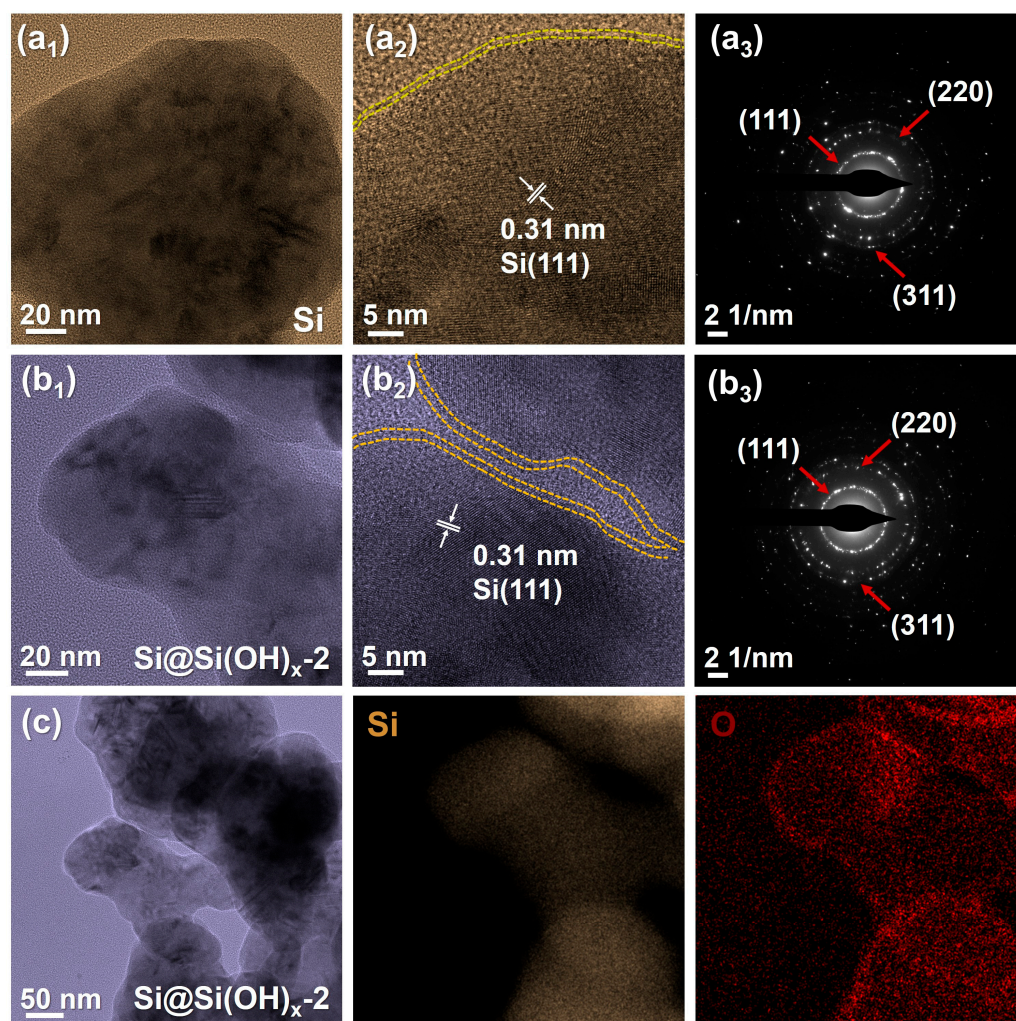


Figure 4. (a₁–b₃) TEM images of a pristine Si particle and the modified Si@Si(OH)_{x-2} nanoparticles by piranha solution, and the corresponding SAED patterns. (c) TEM image and the corresponding EDS elemental mappings of Si@Si(OH)_{x-2} nanoparticles of Si and O.

The differences in electrochemical performances between Si@Si(OH)_x serial samples indicate that controllable introduction of the Si(OH)_x layer could be achieved by adjusting the temperature of the piranha solution. The introduction of an appropriate Si(OH)_x layer could sufficiently improve the hydrophilicity of materials to better disperse and contact with the binders and electrolytes. Furthermore, the Si(OH)_x layer could serve as a protective layer to avoid the pulverization of materials during the charge/discharge process. Table S2 lists the comparisons of our work with those reported works of Si-based materials treated by piranha solution. Generally, recent works in the literature all used piranha solution to introduce the Si(OH)_x layer, however the parameters of treated process are not comprehensively explored. In contrast, we have systematically explored the influences of treated temperature, have achieved the controllable generation of Si(OH)_x layer and

obtaining advanced Si-based anode with excellent electrochemical performance. Actually, excess Si(OH)_x layer is not a beneficial factor for the Si anode. The Si(OH)_x layer itself is an inert and non-conductive layer, and the excess Si(OH)_x layer could alleviate volume expansion of Si, while seriously affecting e^- transport, leading to poor rate performance. Combined with electrochemical performances, the proper introduction of Si(OH)_x layer can be achieved by treating Si with piranha solution at 80°C (Si@Si(OH)_{x-2}), taking into account long cycling stability and rate performance.

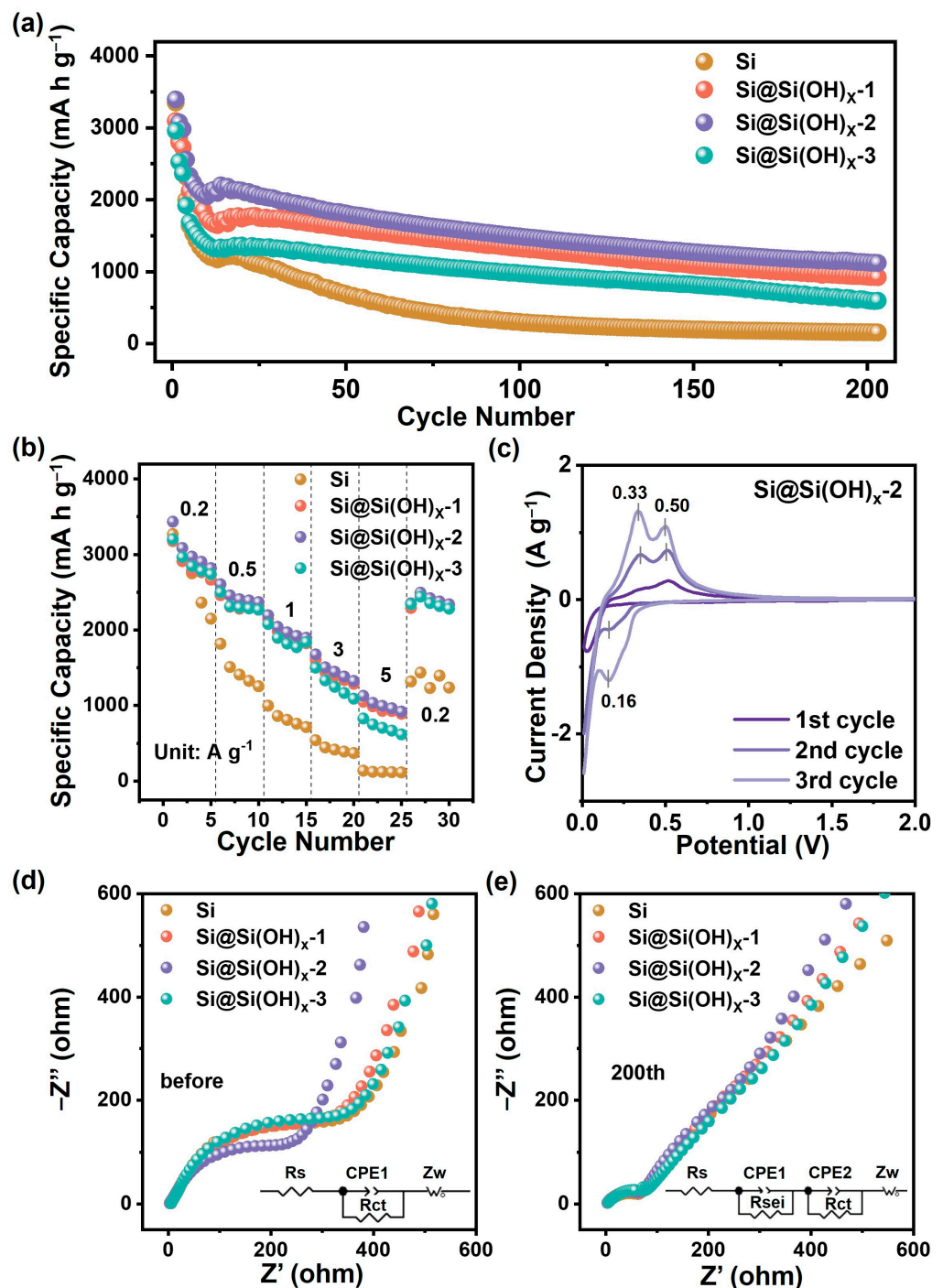


Figure 5. (a) Cycling performances and (b) rate capabilities of Si, Si@Si(OH)_{x-1} , Si@Si(OH)_{x-2} , and Si@Si(OH)_{x-3} anodes. (c) CV curves of the Si@Si(OH)_{x-2} anode at a scan rate of 0.1 mV s^{-1} . Electrochemical impedance patterns of the electrodes (d) before and (e) after 200 cycles of Si, Si@Si(OH)_{x-1} , Si@Si(OH)_{x-2} , and Si@Si(OH)_{x-3} anodes.

Figure 5c displays the CV curves of the Si@Si(OH)_x-2 anode from 0.01 to 2.0 V at a scan rate of 0.1 mV⁻¹. During the initial discharge, the sharp reduction peak in the range of 0.2–0.01 V is attributed to the amorphous Li-Si alloy phase formed by crystalline Si. In both the second and the third negative scans, the new reduction peak evolved at 0.16 V, corresponding to the reversible lithiation process from amorphous Si to Li-Si phase. During the charge process, two oxidation peaks around 0.33 V and 0.50 V occur during the initial sweep cycle and subsequent scan cycles due to the delithiation process of Li–Si to amorphous Si [36,37]. Similar redox behaviors are found in the original Si anode (Figure S5a). Notably, the potential gap between the oxidation and reduction peaks of the Si@Si(OH)_x-2 anode narrows in subsequent cycles compared to the Si anode, indicating the reduction in polarization of the Si@Si(OH)_x-2 anode. In addition, the Si@Si(OH)_x-2 anode displays stronger peak areas, reflecting that Si treated with piranha solution are easier to perform electrochemical reactions. In addition, the cathodic peak at about 1.4 V could be ascribed to the FEC reduction at 1st cycle for the Si and Si@Si(OH)_x-2 anode (Figure S5b).

To further explore the differences in electrochemical performance, the impedance characteristics of Si anodes treated with piranha solution under different conditions were characterized by the EIS. Figure 5d,e shows the EIS patterns and corresponding equivalent circuit models for each anode before cycling and after 200 cycles. The EIS plots of pre-cycle Si, Si@Si(OH)_x-1, Si@Si(OH)_x-2, and Si@Si(OH)_x-3 anode in Figure 5d are all composed of semicircle in the intermediate frequency region (reflecting the charge transfer resistance R_{ct}) and oblique line in the low frequency region (reflecting the lithium-ion diffusion Z_w) [38,39]. The fitted data are shown in Table S3. The R_{ct} of each anode before cycling is 541.5 Ω (Si anode), 516.2 Ω (Si@Si(OH)_x-1 anode), 403.8 Ω (Si@Si(OH)_x-2 anode), and 468.8 Ω (Si@Si(OH)_x-3 anode), respectively. It can be found that the R_{ct} resistance of Si treated with piranha solution is smaller than that of raw Si, while the Si treated with piranha solution at 80 °C exhibits the smallest R_{ct} value, which indicates that the proper introduction of amorphous Si(OH)_x layer is conducive to charge transfer. Meanwhile, as demonstrated in Table S3, the Z_w value of Si treated with piranha solution is lower than that of Si, which indicates that the amorphous Si(OH)_x layer introduced promotes the lithium-ion transport capacity of the anode materials. As shown in Figure 5e, all four samples after 200 cycles exhibit a depressed semicircle in the high-frequency region that reflects the resistance of the SEI film (R_{sei}). As demonstrated in Table S3, the value of R_{sei} of each anode after cycling is 80.76 Ω (Si anode), 76.62 Ω (Si@Si(OH)_x-1 anode), 69.6 Ω (Si@Si(OH)_x-2 anode), and 73.19 Ω (Si@Si(OH)_x-3 anode), respectively. The R_{sei} resistance of the Si treated with piranha solution is smaller than that of the raw silicon, and the sample treated with piranha solution at 80 °C shows the smallest R_{sei} value, which indicates that the introduced amorphous Si(OH)_x layer could inhibit the excessive growth of SEI film to a certain extent. The Z_w value of Si treated with piranha solution is also smaller than that of Si, indicating that the Li⁺ transport rates of anodes treated with piranha solution are faster. The fitting results of Warburg parameter are shown in Figure S6 and Table S4. Si@Si(OH)_x-2 anode exhibits smaller slope than Si and other samples treated by piranha solution, which indicates that the Si@Si(OH)_x-2 anode possesses the best Li⁺ diffusion rate. The EIS results are consistent with the rate capability of anodes, further confirming that piranha solution treatment can improve the electrochemical performances of Si-based anodes.

As illustrated in Figure 6(a₁,b₁), the interfaces and cross sections of Si and Si@Si(OH)_x-2 electrodes before cycling all possess porous interfaces, which is beneficial to fast Li⁺ diffusion and electrolyte penetration. However, the electrode of raw Si has a raised block structure, while Si@Si(OH)_x-2 electrodes show a uniform and flat interface. After 200 cycles, significant cracks are seen in Figure 6(a₂) due to poor cycling stability of Si, which may be caused by the volume expansion of Si during insertion/deinsertion of Li⁺ and deposition of the SEI film, resulting in slow diffusion of Li⁺. In contrast, Figure 6(b₂) shows that only a trace of cracks appeared at the interfaces of the Si@Si(OH)_x-2 electrode treated with piranha solution. From the cross sections diagrams before and after cycles, the raw Si electrode has a large volume expansion, and the cross-section is concave and convex. Compared to

Si, the Si@Si(OH)_{x-2} electrode has only a slight thickness increase, and the cross-sectional shape remains intact. The above discussions confirm that the electrochemical stability of the Si treated with piranha solution has been significantly improved.

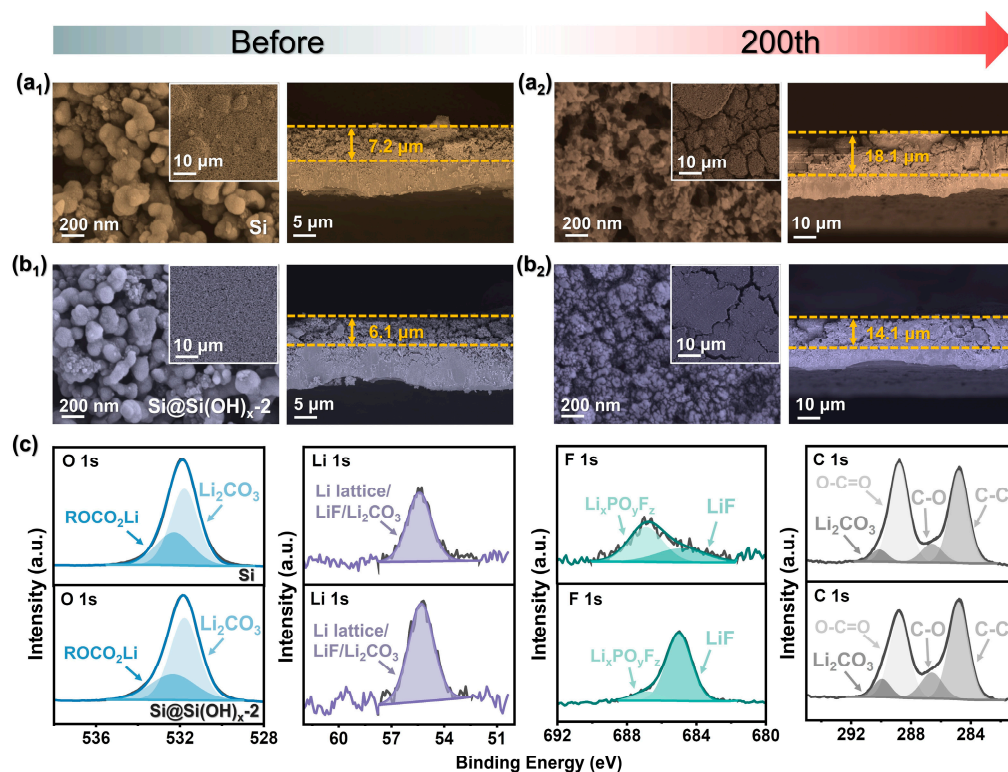


Figure 6. SEM images of the Si electrode (**a₁**) before and (**a₂**) after 200 cycles. SEM images of the Si@Si(OH)_{x-2} electrode (**b₁**) before and (**b₂**) after 200 cycles. (c) XPS spectra of the Si and Si@Si(OH)_{x-2} electrode after 200 cycles.

To further measure the surface elemental composition of the electrode after cycles, XPS were performed after 200 cycles. The full-test scan in Figure S7 shows that after 200 cycles, the elements Li, Si, C, O, and F are present in the Si and Si@Si(OH)_{x-2} electrodes. As shown in Figure 6c, both two electrodes possess four characteristic peaks at 284.8, 286.6, 288.8, and 290 eV in C 1s, corresponding to C-C, C-O, O-C=O bonds, and lithium carbonate (Li₂CO₃) [40]. The intensity of C=O bond on the surface of the modified Si@Si(OH)_{x-2} electrode is weaker than that of Si, which means that the modified electrode surface possesses fewer organic components than Si, which is also observed in O 1s spectrum. The peak intensity of ROCO₂Li corresponding to organic components on the surface of the modified electrode is notably lower than that of Si [41,42]. Ideal Si-based materials will generate a thin and dense SEI film on the surface during cycling. Previous studies have demonstrated that high inorganic components are beneficial for the formation of highly elastic SEI films, such as lithium fluoride (LiF) and Li₂CO₃. As shown in F 1s spectra, both two electrodes exhibit two characteristic peaks at 684.9 and 686.8 eV, corresponding to LiF and Li_xPO_yF_z, respectively [40,43]. The results of XPS show that SEI of the modified Si@Si(OH)_{x-2} electrode possesses LiF-rich inorganic layer and fewer organic components, which is caused by its outstanding cycling stability [44–46].

4. Conclusions

On the whole, we successfully realized the adjustable introduction of the amorphous silicon hydroxyl layer on the Si surface by adjusting the reaction temperature of piranha solution (H₂SO₄/H₂O₂ = 3:1 *v/v*). The optimal sample of Si@Si(OH)_{x-2} corresponded to the Si treated with piranha solution at 80 °C, which exhibited excellent electrochemical per-

formance with a reversible specific capacity of $1121.4 \text{ mA h g}^{-1}$ at 1 A g^{-1} after 200 cycles and an initial Coulomb efficiency of 85.5%. The enhancement of electrochemical performance can be attributed to the controllable introduction of amorphous silicon hydroxyl groups, which could not only greatly improve the dispersion of Si, thus increasing the contact area between the active materials and conductive additives and binders and making electrons/ions easier to transport, but also improve the hydrophilicity of Si to allow the active materials tightly contact with the binders and electrolytes to form robust connection. In addition, the increasing potential of more hydrogen bonds forming between the Si and the hydroxyl-rich SA binders, thereby further enhancing the structural integrity of the electrode. Moreover, the Si@Si(OH)_x -2 anode acquires highly elastic SEI film with rich inorganic components of LiF and Li_2CO_3 as well as lower electrochemical impedance than Si after long cycles. This work delivers a promising and scalable strategy for the surface engineering of nano-Si crystals and has guiding significance for further modification and industrial application of Si-based anodes.

Supplementary Materials: The following supporting information can be downloaded at: <https://www.mdpi.com/article/10.3390/cryst13071127/s1>, Figure S1: Partial enlargement of XRD patterns of Si, Si@Si(OH)_x -1, Si@Si(OH)_x -2, and Si@Si(OH)_x -3 nanoparticles; Table S1: Calculated particles sizes of Si, Si@Si(OH)_x -1, Si@Si(OH)_x -2, and Si@Si(OH)_x -3 based on the Scherrer formula; Figure S2: Raman spectra of Si and Si@Si(OH)_x -2; Figure S3: Photos of Si, Si@Si(OH)_x -1, Si@Si(OH)_x -2, and Si@Si(OH)_x -3 electrodes after contact angle tests; Figure S4: The charge-discharge profiles of Si, Si@Si(OH)_x -1, Si@Si(OH)_x -2, and Si@Si(OH)_x -3 anodes at 1st and 100th cycles; Figure S5: CV curves of (a) the Si anode and (b) the Si and Si@Si(OH)_x -2 anode for 1st cycle at a scan rate of 0.1 mV s^{-1} ; Table S2: The anodic performances comparison of different surface treatment methods; Table S3: The fitting data of the Si, Si@Si(OH)_x -1, Si@Si(OH)_x -2, and Si@Si(OH)_x -3 anodes; Figure S6. $Z' \sim \omega^{-1/2}$ linear relationship diagram of (a) before cycling and (b) after 200 cycles; Table S4: The fitting Warburg parameters of the Si, Si@Si(OH)_x -1, Si@Si(OH)_x -2, and Si@Si(OH)_x -3 anodes; and Figure S7: XPS spectra of the Si and Si@Si(OH)_x -2 electrode after 200 cycles.

Author Contributions: Methodology, T.L.; software, Y.L. and F.Z.; formal analysis, Y.L., F.Z., and N.L.; investigation, Y.L.; resources, T.L., Y.L., F.Z., and N.L.; data curation, T.L.; writing original draft, T.L.; writing review and editing, H.Z., B.C., and L.Y.; visualization, H.Z. and J.Y.; supervision, J.Y., H.Z., B.C., and Y.Y.; project administration, L.Y.; funding acquisition, Y.Y., L.Y., and F.Z. All authors have read and agreed to the published version of the manuscript.

Funding: This work was supported partially by the National Key Research and Development Program (No. 2022YFC3900905), the National Natural Science Foundation of China (Nos. 52234001, 62104703, and 52074119), the Science and Technology Planning Project of Hunan Province (No. 2018TP1017), the Scientific Research Fund of Hunan Provincial Education Department (No. 22A0045), the Science and Technology Innovation Program of Hunan Province (No. 2021RC1003), the Changsha Science and Technology Foundation (No. kq2208162) and Joint Funds of Hunan Provincial Innovation Foundation for Post-graduate (No. CX20220512), Natural Science Research Start-up Foundation of Recruiting Talents of Nanjing University of Posts and Telecommunications (Grant No. NY223016), the Project of State Key Laboratory of Organic Electronics and Information Displays, Nanjing University of Posts and Telecommunication.

Data Availability Statement: Data underlying the results presented in this paper are not publicly available at this time but may be obtained from the authors upon reasonable request.

Conflicts of Interest: The authors declare no conflict of interest.

References

1. Wang, Q.L.; Kang, L.B.; Xing, Z.; Nie, C.H.; Hong, H.P.; Zhou, X.C.; Yun, Q.B.; Ju, Z.C.; Chen, B. Prussian blue analogue-derived $\text{ZnO/ZnFe}_2\text{O}_4$ core-shell nanospheres as high-performance anodes for lithium-ion and potassium-ion batteries. *Batter. Supercaps* **2023**, *6*, e202200411. [[CrossRef](#)]
2. Zhao, Z.D.; Sun, M.Q.; Wu, T.Q.; Zhang, J.J.; Wang, P.; Zhang, L.; Yang, C.Y.; Peng, C.G.; Lu, H.B. A bifunctional-modulated conformal Li/Mn-rich layered cathode for fast-charging, high volumetric density and durable Li-ion full cells. *Nano-Micro Lett.* **2021**, *13*, 118. [[CrossRef](#)]

3. Zhu, Y.S.; Wang, C.T.; Cheng, Z.J.; Yao, Q.; Su, J.; Chen, B.; Yang, J.; Qian, Y.T. Bimetallic Bi–Sn microspheres as high initial Coulombic efficiency and long lifespan anodes for sodium-ion batteries. *Chem. Commun.* **2022**, *58*, 5140–5143. [[CrossRef](#)]
4. Chu, Y.; Xiong, S. Mixed transition-metal oxides@carbon core-shell nanostructures derived from heterometallic clusters for enhanced lithium storage. *Chin. Chem. Lett.* **2022**, *33*, 486–490. [[CrossRef](#)]
5. Li, P.; Kim, H.; Myung, S.T.; Sun, Y.K. Diverting exploration of silicon anode into practical way: A review focused on silicon-graphite composite for lithium ion batteries. *Energy Storage Mater.* **2021**, *35*, 550–576. [[CrossRef](#)]
6. Ge, M.; Cao, C.; Biesold, M.G.; Sewell, C.D.; Hao, S.M.; Huang, J.; Zhang, W.; Lai, Y.; Lin, Z. Recent advances in silicon-based electrodes: From fundamental research toward practical applications. *Adv. Mater.* **2021**, *33*, 2004577. [[CrossRef](#)]
7. Cheng, H.; Shapter, J.G.; Li, Y.; Gao, G. Recent progress of advanced anode materials of lithium-ion batteries. *J. Energy Chem.* **2021**, *57*, 451–468. [[CrossRef](#)]
8. Shi, Q.; Zhou, J.; Ullah, S.; Yang, X.; Tokarska, K.; Trzebicka, B.; Ta, H.Q.; Rummeli, M.H. A review of recent developments in Si/C composite materials for Li-ion batteries. *Energy Storage Mater.* **2021**, *34*, 735–754. [[CrossRef](#)]
9. Zhang, L.; Zhu, C.; Yu, S.; Ge, D.; Zhou, H. Status and challenges facing representative anode materials for rechargeable lithium batteries. *J. Energy Chem.* **2022**, *66*, 260–294. [[CrossRef](#)]
10. Zhang, Y.; Wu, B.; Mu, G.; Ma, C.; Mu, D.; Wu, F. Recent progress and perspectives on silicon anode: Synthesis and prelithiation for LIBs energy storage. *J. Energy Chem.* **2022**, *64*, 615–650. [[CrossRef](#)]
11. Zhou, J.; Lu, Y.; Yang, L.; Zhu, W.; Liu, W.; Yang, Y.; Liu, K. Sustainable silicon anodes facilitated via a double-layer interface engineering: Inner SiO_x combined with outer nitrogen and boron co-doped carbon. *Carbon Energy* **2022**, *4*, 399–410. [[CrossRef](#)]
12. Zhang, F.; Zhu, W.; Li, T.T.; Yuan, Y.; Yin, J.; Jiang, J.; Yang, L.S. Advances of synthesis methods for porous silicon-based anode materials. *Front. Chem.* **2022**, *10*, 889563. [[CrossRef](#)]
13. Jung, C.H.; Kim, K.H.; Hong, S.H. Stable silicon anode for lithium-ion batteries through covalent bond formation with a binder via esterification. *ACS Appl. Mater. Interfaces* **2019**, *11*, 26753–26763. [[CrossRef](#)]
14. Chou, C.Y.; Kuo, J.R.; Yen, S.C. Silicon-based composite negative electrode prepared from recycled silicon-slicing slurries and lignin/lignocellulose for Li-ion cells. *ACS Sustain. Chem. Eng.* **2018**, *6*, 4759–4766. [[CrossRef](#)]
15. Zhang, M.Y.; Liang, N.W.; Hao, D.; Chen, Z.X.; Zhang, F.; Yin, J.; Yang, Y.H.; Yang, L.S. Recent advances of SiO_x-based anodes for sustainable lithium-ion batteries. *Nano Res. Energy* **2023**, *2*, 9120077. [[CrossRef](#)]
16. Zhang, J.; Zhang, F.; Zhu, W.; Xi, X.; Yang, L.; Tu, F.; Feng, Q.; Li, T.; Yang, Y.; Yang, L. Restricted-magnesium-vapor-reduction of amorphous SiO/C precursors to polycrystalline Si/SiO_x/C hybrid anodes. *Chem. Commun.* **2023**, *59*, 1169–1172. [[CrossRef](#)]
17. Zhou, L.; Ma, W.; Yang, L.; Shao, L.; Zhou, J.; Yang, C.; Liu, X.; Xi, X. A hierarchically structured Si/Cu/Ag integrated anode for efficient lithium-ion batteries. *Mater. Lett.* **2019**, *244*, 199–202. [[CrossRef](#)]
18. Li, C.; Shi, T.; Li, D.; Yoshitake, H.; Wang, H. Effect of surface modification on electrochemical performance of nano-sized Si as an anode material for Li-ion Batteries. *RSC Adv.* **2016**, *6*, 34715–34723. [[CrossRef](#)]
19. Zhang, C.; Wang, F.; Han, J.; Bai, S.; Tan, J.; Liu, J.S.; Li, F. Challenges and recent progress on silicon-based anode materials for next-generation lithium-ion batteries. *Small Struct.* **2021**, *2*, 2100009. [[CrossRef](#)]
20. Zhao, X.Y.; Lehto, V.P. Challenges and prospects of nanosized silicon anodes in lithium-ion batteries. *Nanotechnology* **2020**, *32*, 042002. [[CrossRef](#)] [[PubMed](#)]
21. Zhu, W.; Zhou, J.; Xiang, S.; Bian, X.; Yin, J.; Jiang, J.; Yang, L. Progress of binder structures in silicon-based anodes for advanced lithium-ion batteries: A mini review. *Front. Chem.* **2021**, *9*, 712225. [[CrossRef](#)] [[PubMed](#)]
22. Luo, W.; Chen, X.; Xia, Y.; Chen, M.; Wang, L.; Wang, Q.; Li, W.; Yang, J. Surface and interface engineering of silicon-based anode materials for lithium-ion batteries. *Adv. Energy Mater.* **2017**, *7*, 1701083. [[CrossRef](#)]
23. Zhao, H.; Wei, Y.; Qiao, R.; Zhu, C.; Zheng, Z.; Ling, M.; Jia, Z.; Bai, Y.; Fu, Y.; Lei, J.; et al. Conductive polymer binder for high-tap-density nanosilicon material for lithium-ion battery negative electrode application. *Nano Lett.* **2015**, *15*, 7927–7932. [[CrossRef](#)] [[PubMed](#)]
24. Scheeler, S.P.; Ullrich, S.; Kudera, S.; Pacholski, C. Fabrication of porous silicon by metal-assisted etching using highly ordered gold nanoparticle arrays. *Nanoscale Res. Lett.* **2012**, *7*, 450. [[CrossRef](#)]
25. Zhao, G.; Zhang, L.; Meng, Y.; Zhang, N.; Sun, K. Decoration of graphene with silicon nanoparticles by covalent immobilization for use as anodes in high stability lithium ion batteries. *J. Power Source* **2013**, *240*, 212–218. [[CrossRef](#)]
26. Koh, K.S.; Chin, J.; Chia, J.; Chiang, C.L. Quantitative studies on PDMS-PDMS interface bonding with piranha solution and its swelling effect. *Micromachines* **2012**, *3*, 427–441. [[CrossRef](#)]
27. Guo, S.; Li, H.; Li, Y.; Han, Y.; Chen, K.; Xu, G.; Zhu, Y.; Hu, X. SiO₂-Enhanced structural stability and strong adhesion with a new binder of konjac glucomannan enables stable cycling of silicon anodes for lithium-ion batteries. *Adv. Energy Mater.* **2018**, *8*, 1800434. [[CrossRef](#)]
28. Zuo, X.; Chang, K.; Zhao, J.; Xie, Z.; Tang, H.; Li, B.; Chang, Z. Bubble-template-assisted synthesis of hollow fullerene-like MoS₂ nanocages as a lithium ion battery anode material. *J. Mater. Chem. A* **2016**, *4*, 51–58. [[CrossRef](#)]
29. Zhu, Y.; Liu, W.; Zhang, X.; He, J.; Chen, J.; Wang, Y.; Cao, T. Directing silicon-graphene self-assembly as a core/shell anode for high-performance lithium-ion batteries. *Langmuir* **2013**, *29*, 744–749. [[CrossRef](#)]
30. Ai, Q.; Li, D.; Guo, J.; Hou, G.; Sun, Q.; Sun, Q.; Xu, X.; Zhai, W.; Zhang, L.; Feng, J.; et al. Artificial solid electrolyte interphase coating to reduce lithium trapping in silicon anode for high performance lithium-ion batteries. *Adv. Mater. Interfaces* **2019**, *6*, 1901187. [[CrossRef](#)]

31. DuMont, J.W.; Marquardt, A.E.; Cano, A.M.; George, S.M. Thermal atomic layer etching of SiO₂ by a “conversion-etch” mechanism using sequential reactions of trimethylaluminum and hydrogen fluoride. *ACS Appl. Mater. Interfaces* **2017**, *9*, 10296–10307. [[CrossRef](#)] [[PubMed](#)]
32. Li, Q.; Chen, D.; Li, K.; Wang, J.; Zhao, J. Electrostatic self-assembly BmSi@C/RGO composite as anode material for lithium ion battery. *Electrochim. Acta* **2016**, *202*, 140–146. [[CrossRef](#)]
33. Zhou, J.; Zhou, L.; Yang, L.; Chen, T.; Li, J.; Pan, H.; Yang, Y.; Wang, Z. Carbon free silicon/polyaniline hybrid anodes with 3D conductive structures for superior lithium-ion batteries. *Chem. Commun.* **2020**, *56*, 2328–2331. [[CrossRef](#)]
34. Liu, W.; Liu, J.; Zhu, M.; Wang, W.; Wang, L.; Xie, S.; Wang, L.; Yang, X.; He, X.; Sun, Y. Recycling of lignin and Si waste for advanced Si/C battery anodes. *ACS Appl. Mater. Interfaces* **2020**, *12*, 57055–57063. [[CrossRef](#)]
35. Jung, C.H.; Kim, K.H.; Hong, S.H. An in situ formed graphene oxide-polyacrylic acid composite cage on silicon microparticles for lithium ion batteries via an esterification reaction. *J. Mater. Chem. A* **2019**, *7*, 12763–12772. [[CrossRef](#)]
36. Liu, J.; Zhang, Q.; Zhang, T.; Li, J.T.; Huang, L.; Sun, S.G. A robust ion-conductive biopolymer as a binder for Si anodes of lithium-ion batteries. *Adv. Funct. Mater.* **2015**, *25*, 3599–3605. [[CrossRef](#)]
37. Zhu, W.; Zhou, J.; Zhang, F.; Li, T.; Yang, Y.; Yin, J.; Tian, Z.; Li, W.; Lai, Y.; Yang, L. Sustainable silicon micro-dendritic anodes integrated by a moderately cross-linked polymer binder with superior elasticity and adhesion. *J. Alloys Compd.* **2022**, *926*, 166858. [[CrossRef](#)]
38. Yue, L.; Zhang, L.; Zhong, H. Carboxymethyl chitosan: A new water soluble binder for Si anode of Li-ion batteries. *J. Power Source* **2014**, *247*, 327–331. [[CrossRef](#)]
39. Cen, Y.; Qin, Q.; Sisson, R.D.; Liang, J. Effect of particle size and surface treatment on Si/graphene nanocomposite lithium-ion battery anodes. *Electrochim. Acta* **2017**, *251*, 690–698. [[CrossRef](#)]
40. Kang, H.; Song, M.; Yang, M.; Lee, J. Lithium metal anode with lithium borate layer for enhanced cycling stability of lithium metal batteries. *J. Power Source* **2021**, *485*, 229286. [[CrossRef](#)]
41. Hu, W.; Zhang, C.; Jiang, H.; Zheng, M.; Wu, Q.H.; Dong, Q. Improving the electrochemistry performance of layer LiNi_{0.5}Mn_{0.3}Co_{0.2}O₂ material at 4.5 V cutoff potential using lithium metaborate. *Electrochim. Acta* **2017**, *243*, 105–111. [[CrossRef](#)]
42. Wang, D.; Li, X.; Wang, Z.; Guo, H.; Chen, X.; Zheng, X.; Xu, Y.; Ru, J. Multifunctional Li₂O-2B₂O₃ coating for enhancing high voltage electrochemical performances and thermal stability of layered structured LiNi_{0.5}Co_{0.2}Mn_{0.3}O₂ cathode materials for lithium ion batteries. *Electrochim. Acta* **2015**, *174*, 1225–1233. [[CrossRef](#)]
43. Zhao, R.; Liang, J.; Huang, J.; Zeng, R.; Zhang, J.; Chen, H.; Shi, G. Improving the Ni-Rich LiNi_{0.5}Co_{0.2}Mn_{0.3}O₂ cathode properties at high operating voltage by double coating layer of Al₂O₃ and AlPO₄. *J. Alloys Compd.* **2017**, *724*, 1109–1116. [[CrossRef](#)]
44. Koo, B.; Kim, H.; Cho, Y.; Lee, K.T.; Choi, N.S.; Cho, J. A highly cross-linked polymeric binder for high-performance silicon negative electrodes in lithium ion batteries. *Angew. Chem.* **2012**, *124*, 8892–8897. [[CrossRef](#)]
45. Huey, Z.; Ha, Y.; Frisco, S.; Norman, A.; Teeter, G.; Jiang, C.S.; DeCaluwe, S.C. Multi-modal characterization methods of solid-electrolyte interphase in silicon-graphite composite electrodes. *J. Power Source* **2023**, *564*, 232804. [[CrossRef](#)]
46. Tan, J.; Matz, J.; Dong, P.; Shen, J.; Ye, M. A Growing appreciation for the role of LiF in the solid electrolyte interphase. *Adv. Energy Mater.* **2021**, *11*, 2100046. [[CrossRef](#)]

Disclaimer/Publisher’s Note: The statements, opinions and data contained in all publications are solely those of the individual author(s) and contributor(s) and not of MDPI and/or the editor(s). MDPI and/or the editor(s) disclaim responsibility for any injury to people or property resulting from any ideas, methods, instructions or products referred to in the content.